Orientation and Penetration Depth of Monolayer-Bound p40^{phox}-PX†

Šárka Málková,‡ Robert V. Stahelin,§ Sai V. Pingali,‡ Wonhwa Cho,§ and Mark L. Schlossman*,‡,§

Departments of Physics and Chemistry, University of Illinois, Chicago, Illinois 60607

Received June 7, 2006; Revised Manuscript Received September 11, 2006

ABSTRACT: X-ray reflectivity was used to study the interaction of the PX domain of p40^{phox} protein (p40^{phox}-PX) with a Langmuir monolayer of a mixture of SOPC (1-stearoyl-2-oleoyl-*sn*-glycero-3-phosphocholine), SOPS (1-stearoyl-2-oleoyl-*sn*-glycero-3-phosphoserine), and DPPtdIns(3)P (1,2-dipalmitoylphosphatidylinositol 3-phosphate) lipids supported on a buffered aqueous solution. The reflectivity is analyzed in terms of the known crystallographic structure of the p40^{phox}-PX domain and a slab model that represents the lipid layer, yielding an electron density profile of the lipid layer and bound PX domains. This analysis determines the angular orientation and penetration depth of the p40^{phox}-PX domain bound to the SOPC/SOPS/DPPtdIns(3)P monolayer. The best fit orientation is characterized by the following angles: $\theta = 30 \pm 10°$ and $\phi = 140 \pm 30°$. These angles describe rotations, about axes in a coordinate system fixed to the domain, that are required to orient the domain with respect to the lipid layer at the interface. The protein penetrated into the lipid layer by 9 ± 2 Å, indicating that the protein penetrated into the headgroup region, but not deeply into the hydrocarbon region of the monolayer. In this analysis, polar Tyr^{94} and hydrophobic Val^{95} penetrated deepest into the lipid monolayer. The backbone of these residues was ∼5 Å above the headgroup−buffer interface, i.e., at the level of the SOPC/SOPS lipid phosphates. Positively charged Lys^{92} and Lys^{98} were also near the SOPC/SOPS lipid phosphates. This position of the protein allows for a favorable electrostatic contribution to binding.

Many cellular proteins involved in cell signaling and vesicle trafficking are specifically targeted to different cell membranes in response to various stimuli, including calcium and lipid mediators (*1*−*3*). A growing body of evidence indicates that phosphorylated derivatives of phosphatidylinositol (PtdIns), collectively known as phosphoinositides (PIs),[1] serve as site-specific membrane signals in recruiting and activating a variety of cellular proteins (*4*, *5*). The molecular mechanisms by which different PIs modulate the membrane targeting and activation of these proteins are just starting to be revealed as structural information about the membrane targeting domains that bind different types of PIs becomes available.

Studies have indicated that much of the subcellular targeting of these membrane targeting domains can be ascribed to biophysical principles that govern their binding to model membranes in vitro. Recently, one of us (W.C.) investigated the membrane targeting by PI-binding domains, including FYVE (Fablp, YOTB, Vac1p, and EEA1) (*6*), PX (Phox) (*7*), and ENTH/ANTH (epsin or adaptor protein N-terminal homology) domains (*8*). This work demonstrated, for example, the mechanism by which phosphatidylinositol 3,4-bisphosphate [PtdIns(3,4)P_2] induces membrane targeting and penetration of the PX domain of p47^{phox} of NADPH oxidase (*7*).

The PX domain is composed of 100−140 amino acids and was first identified in two cytosolic components, p47^{phox} and p40^{phox}, of NADPH oxidase (*9*). It has been found in a variety of proteins involved in cell signaling and membrane trafficking, such as class II PI3-kinase, phospholipase D, cytokine-independent survival kinase (CISK), Vam7 SNARE protein, and all members of the sorting nexin family (SNX1−16) (*9*). The p40^{phox}-PX domain was shown to be localized at PtdIns(3)P-rich endosomes when expressed ectopically in mammalian cells (*10*, *11*). Many PX domains, including those from p40^{phox} (*10*, *12*), Vam7p (*13*), and sorting nexin 3 (*14*), have been found to specifically interact with PtdIns(3)P. The recently determined X-ray crystal structure of the p40^{phox}-PX domain bound to water-soluble DBuPtdIns(3)P (1,2-dibutanoylphosphatidylinositol 3-phosphate) illustrated how the domain achieves stereospecific recognition of PtdIns(3)P (*10*). The structure revealed that basic residues, Lys^{92} and Arg^{58} (conserved among many PX domains), form

† This work was supported by NIH Grants GM52598 and GM68849 (W.C.) and NSF Grant CHE0315691 (M.L.S.). Brookhaven National Laboratory is supported by the U.S. Department of Energy.

* To whom correspondence should be addressed: Department of Physics, University of Illinois, Chicago, IL 60607-7059. E-mail: schloss@uic.edu. Telephone: (312) 996-8787. Fax: (312) 996-9016.

‡ Department of Physics.

§ Department of Chemistry.

[1] Abbreviations: cPLA$_2$α-C2, C2 domain of cytosolic phospholipase A$_2$α; DBuPtdIns(3)P, 1,2-dibutanoylphosphatidylinositol 3-phosphate; DOPC, 1,2-dioleoyl-*sn*-glycero-3-phosphocholine; DPPC, 1,2-dipalmitoyl-*sn*-glycero-3-phosphocholine; DPPtdIns(3)P, 1,2-dipalmitoylphosphatidylinositol 3-phosphate; EEA1, early endosome antigen 1; EPR, electron paramagnetic resonance; HEPES, *N*-(2-hydroxyethyl)piperazine-*N*′-2-ethanesulfonic acid; NMR, nuclear magnetic resonance; p40^{phox}-PX domain, PX domain of p40^{phox} protein; PDB, Protein Data Bank; PI, phosphoinositide; POPC, 1-palmitoyl-2-oleoyl-*sn*-glycero-3-phosphocholine; POPE, 1-palmitoyl-2-oleoyl-*sn*-glycero-3-phosphoethanolamine; PtdIns(3)P, phosphatidylinositol 3-phosphate; SOPC, 1-stearoyl-2-oleoyl-*sn*-glycero-3-phosphocholine; SOPS, 1-stearoyl-2-oleoyl-*sn*-glycero-3-phosphoserine.

10.1021/bi061133l CCC: $33.50
Published on Web 10/20/2006

hydrogen bonds with the 1- and 3-phosphate of PtdIns(3)P, respectively.

Since the function and regulation of a majority of peripheral proteins depend upon their interactions with membranes, it is important to determine the structural arrangement of peripheral proteins and membrane targeting domains at the membrane, including their membrane-bound orientation and depth of penetration. Although measurements of the level of membrane binding of p40^{phox}-PX and respective mutants by surface plasmon resonance and monolayer techniques as well as electrostatic potential calculations (*15*) provided insight into the membrane targeting mechanisms of p40^{phox}-PX, these techniques do not provide a quantitative measurement of the protein's orientation and penetration. A high-resolution structure of a protein bound to a bilayer or monolayer containing phosphoinositides has not been determined because of difficulties encountered in crystallizing peripheral proteins in the presence of lipid bilayers. However, recent advances in NMR, EPR, and X-ray reflectivity have allowed characterization of the bound structure. Kutateladze and co-authors recently characterized the binding of the PtdIns(3)P-bound early endosome antigen 1 (EEA1) FYVE domain to micelles using labeled lipids and NMR (*16*, *17*). They determined quantitatively one of the two angles required to specify the orientation and also determined qualitatively the penetration depth. EPR measurements on a spin-labeled C2 domain of cytosolic phospholipase $A_2\alpha$ (cPLA$_2\alpha$-C2) determined values of two angles of orientation and its penetration depth (*18*, *19*), though extensive labeling of the protein was required.

To characterize the membrane penetration of proteins, we introduced the use of protein crystallographic information into the analysis of X-ray reflectivity. X-ray reflectivity measurements had been used previously to study peripheral proteins interacting with a lipid monolayer at the air−water interface (*20*−*25*). This technique, which does not require proteins or lipids to be crystallized or labeled, determines the electron density profile along the surface normal. The profile describes the lipid monolayer and the bound proteins. Our new analysis method allowed us to determine the penetration depth and angular orientation of cPLA$_2\alpha$-C2 bound to a lipid monolayer of 1-stearoyl-2-oleoyl-*sn*-glycero-3-phosphocholine (SOPC) (*26*). These results were in qualitative, though not quantitative, agreement with the bound structure determined by EPR measurements (*18*, *19*). Here, we apply this analysis method to an X-ray reflectivity study of p40^{phox}-PX bound to a mixed monolayer of SOPC, SOPS (1-stearoyl-2-oleoyl-*sn*-glycero-3-phosphoserine), and DPPtdIns(3)P (1,2-dipalmitoylphosphatidylinositol 3-phosphate) at the surface of an aqueous buffer. By determining the membrane penetration and orientation of p40^{phox}-PX, our analysis deduces the location of the most deeply penetrating residues, Tyr^{94} and Val^{95}, the proximity of these residues to the lipid phosphates, and the location of the positively charged residues, Lys^{92} and Lys^{98}, within the headgroup region.

MATERIALS AND METHODS

Materials. KCl and HEPES from Fisher Scientific and EGTA from Sigma were used as obtained. The stock solution of SOPC and SOPS (7:3 molar ratio) in chloroform and 1-palmitoyl-2-{6-[(7-nitro-2-1,3-benzoxadiazol-4-yl)amino]-hexanoyl}-*sn*-glycero-3-phosphocholine in chloroform were purchased from Avanti Polar Lipids, Inc. (Alabaster, AL) and used without further purification. DPPtdIns(3)P was synthesized as described previously (*27*). Spreading solution was made by diluting the SOPC/SOPS stock solution with chloroform from freshly opened bottles (Sigma) and vortexing to mix the DPPtdIns(3)P into this solution. The expression and purification of the PX domain of p40^{phox} were carried out as described previously (*15*).

Pressure and Fluorescence Microscopy Measurements. The change in surface pressure π upon adsorption of protein to the lipid monolayer was measured at a constant surface area using a 10 mL circular Teflon trough andWilhelmy plate connected to a Cahn microbalance, as described previously (*28*). A lipid monolayer containing SOPC, SOPS, and DPPtdIns(3)P (63:27:10) was spread onto the subphase [0.16 M KCl and 10 mM HEPES buffer (pH 7.4)] until the desired initial surface pressure (π_0) was reached. After the pressure stabilized (≈30 min), p40^{phox}-PX was injected into the subphase, and surface pressure π was monitored for 45 min while the subphase was stirred at 60 rpm with a Teflon stir bar. Typically, π stabilized after 30 min. The change in surface pressure $\Delta\pi$ ($\Delta\pi = \pi - \pi_0$) depended upon the protein concentration and saturated at a protein concentration of 6 μg/mL. The protein concentration in the subphase was maintained above this value for the reported experiments. The uncertainty in $\Delta\pi$ was ±0.5 mN/m.

Fluorescence microscopy was used to verify the absence of domains in both the SOPC/SOPS/DPPtdIns(3)P monolayer and the SOPC/SOPS/DPPtdIns(3)P/p40^{phox}-PX system. One mole percent fluorescent dye (1-palmitoyl-2-{6-[(7-nitro-2-1,3-benzoxadiazol-4-yl)amino]hexanoyl}-*sn*-glycero-3-phosphocholine) was mixed into the SOPC/SOPS/DPPtdIns(3)P solution for visualization of the monolayer.

X-ray Reflectivity Measurements. We reported earlier the conditions required for measuring the X-ray reflectivity from a Langmuir monolayer of unsaturated lipids (mainly SOPC) with negligible X-ray damage for a period of up to 8 h (*26*). The same methodology was followed here to measure the reflectivity from the SOPC/SOPS/DPPtdIns(3)P monolayer-bound p40^{phox}-PX. A period of 8 h was sufficiently long to measure the reflectivity from the SOPC/SOPS/DPPtdIns(3)P monolayer, inject p40^{phox}-PX domains into the subphase, allow the domains to bind to the SOPC/SOPS/DPPtdIns-(3)P monolayer, and remeasure the reflectivity to determine the structural arrangement of the domains bound to the monolayer.

X-ray reflectivity experiments were carried out at beamline X19C at the National Synchrotron Light Source (Brookhaven National Laboratory, Upton, NY) with a liquid surface spectrometer described in detail elsewhere (*29*). Reflectivity was measured as a function of the wave vector transfer, Q_z, by varying incident angle α (measured from the plane of the buffer surface) and measuring the intensity of scattered X-rays at reflected angle α (see Figure 1). The wave vector transfer of the reflected X-rays, $\vec{Q}$, was solely in the *z*-direction normal to the buffer surface with a magnitude given by the relation $Q_z = (4\pi/\lambda)\sin(\alpha)$, where λ (1.54 ± 0.003 Å) was the X-ray wavelength used in these measurements. Reflectivity probes variations in structure as a function of the depth of penetration into the surface.

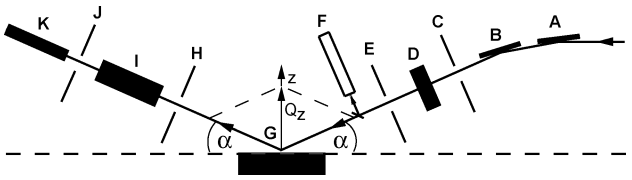

FIGURE 1: Schematic diagram of the experimental setup at X-ray beamline X19C, National Synchrotron Light Source (Brookhaven National Laboratory): (A) focusing mirror, (B) monochromator, (C, E, H, and J) slits, (D) aluminum absorbers, (F) X-ray monitor, (G) sample trough, (I) detector absorbers, and (K) scintillation X-ray detector. The reflected angle was equal to incident angle α, and the reflected X-rays were in the plane of incidence. The only nonzero component of the wave vector transfer was its *z* component (*z* axis normal to the buffer surface), which is given by the equation $Q_z = (4\pi/\lambda)\sin(\alpha)$, where λ was the wavelength of the incident X-rays.

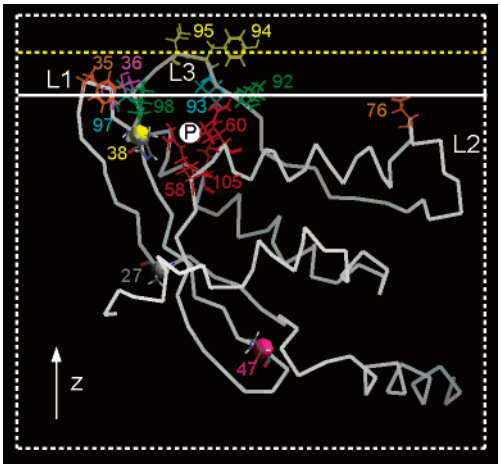

FIGURE 2: Crystal structure of p40^{phox}-PX. The protein is in the best fit orientation defined by a θ of 30° and a φ of 140°, with the *z* axis indicated. The solid white line represents an $x-y$ plane separating the bottom of the lipid layer and the buffer, and the yellow dashed line is 5 Å above the white line and indicates the mean depth of the phosphate groups of SOPC and SOPS. The part of the protein above the solid white line penetrates into the SOPC/SOPS/DPPtdIns(3)P monolayer. The first, second, and third reference atoms are shown as pink, yellow, and gray spheres, respectively. The selected atoms are the α-carbons in residues Thr^{47} (pink), His^{38} (yellow), and Ala^{27} (gray). Loops L1, L2, and L3 (see the text) are marked. The letter P in a white circle indicates the position of the 3-phosphate in PtdIns(3)P in the p40^{phox}-PX binding site as given by ref *10*.

The reflectivity, $R(Q_z)$, represents the scattered intensity normalized by the X-ray intensity measured immediately before the sample. In addition, background scattering was measured and subtracted as described elsewhere (*29*). To make the features of the reflectivity curve more evident, $R(Q_z)$ was divided by $R_F(Q_z)$, the Fresnel reflectivity calculated for an ideal, smooth, and flat interface between the bulk buffer and vapor (*30*). Deviations of the measured reflectivity, $R(Q_z)$, from the Fresnel reflectivity, $R_F(Q_z)$, revealed the presence of interfacial structure as a function of the depth of penetration into the surface. In this case, the structure was due to the lipid monolayer supported on the buffer surface and to p40^{phox}-PX bound to the lipid monolayer. Reflectivity data were analyzed using the Parratt recursive algorithm (*31*). The models chosen to describe the pure lipid monolayer and the lipid/protein system were described in detail by Málková et al. (*26*).

To prepare a typical sample for X-ray reflectivity study, approximately 10 μL of a 1 mM solution of SOPC, SOPS, and DPPtdIns(3)P (63:27:10) in chloroform was added dropwise onto the surface of a 10 mM HEPES buffer (pH 7.4) containing 0.16 M KCl in a 72 mm diameter circular Teflon trough (total volume of ca. 40 mL). The resulting lipid monolayer (at a surface pressure π of ≈26 mN/m) was equilibrated for 2 h (the sample was not stirred during this time), and the reflectivity was measured. An amount greater than that required to saturate the lipid with adsorbed p40^{phox}-PX (i.e., >240 μg) was injected into the subphase; the system was equilibrated for 1 h with continuous slow stirring, and the reflectivity was measured. The surface pressure was monitored to ensure the integrity of the monolayer during the X-ray experiment. Typical variations in surface pressure were less than 1 mN/m during the period of the measurement.

Due to their unsaturated nature, SOPC and SOPS lipids are prone to oxidation and radiation damage. Even without X-ray exposure, there was a small decrease in the surface pressure if it was monitored for a long time (on the order of 1 mN/m over 24 h). X-ray reflectivity measurements of the SOPC/SOPS/DPPtdIns(3)P monolayer and the SOPC/SOPS/DPPtdIns(3)P monolayer with bound p40^{phox}-PX had to be completed before the lipid monolayer deteriorated. To decrease the total time for the experiment, the initial measurement of the SOPC/SOPS/DPPtdIns(3)P monolayer was taken with a small number of data points. Our experience shows that the lipid reflectivity curve has a well-defined shape; therefore, a small number of data points at carefully chosen values of Q_z determines the whole curve. Measurements of the lipid/protein system contained more data points (see ref *26* for further details of the measurement). No radiation damage was detected during the measurements, as indicated by the surface pressure stability and reproducibility of the X-ray reflectivity data after repeated measurements on the same sample.

In our geometry, the lipid monolayer was in the $x-y$ plane and the *z* axis was perpendicular to the monolayer. We defined a second coordinate system, attached to the protein, to describe the protein orientation with respect to the lipid monolayer (*26*). Three atoms were chosen as reference points. The first and second atoms were located in the longest β-strand of the domain (strand β2), and the third atom was located in strand β1. The selected atoms were the α-carbons of residues Thr^{47}, His^{38}, and Ala^{27} (see Figure 2). Two molecular vectors were then defined, a z' vector extending from the first atom (in Thr^{47}) to the second atom (in His^{38}) and an x' vector passing through the third atom (in Ala^{27}) and perpendicular to the first vector. A molecular coordinate system was then defined, with its center at the first α-carbon, the z' axis parallel to the z' vector, and the x' axis parallel to the x' vector. The orientation of the y' axis (perpendicular to the $x'-z'$ plane) was defined by the requirement of a right-handed $x'y'z'$ coordinate system. The domain was then oriented relative to an imaginary planar membrane surface in two different ways. First, the domain was placed in a common starting orientation with its z' axis normal to the membrane. This placed the calibration β2 strand perpendicular to the membrane surface. Second, the domain was placed in its final bound orientation. Last, the transformations needed to change the starting orientation into the final orientation were calculated as a rotation about the x' axis by angle θ followed by a rotation about the z' axis by angle φ.

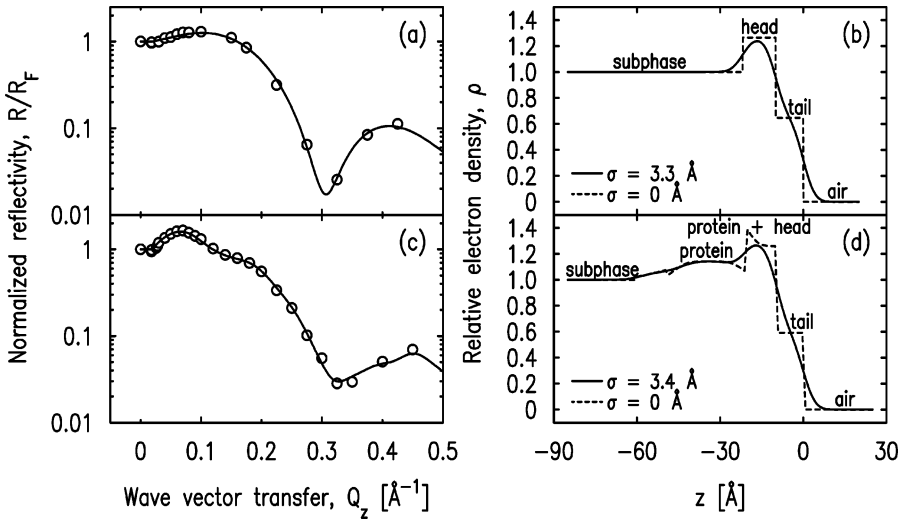

FIGURE 3: (a and b) Normalized X-ray reflectivity and interfacial electron density profile of the pure SOPC/SOPS/DPPtdIns(3)P monolayer at $\pi = 25.9$ mN/m. (c and d) Normalized X-ray reflectivity and interfacial electron density profile of the SOPC/SOPS/DPPtdIns(3)P monolayer-bound p40^{phox}-PX system. Empty circles in panels a and c represent the experimental X-ray reflectivity data, and solid lines represent the best fit of the data using models described in the text. The corresponding fit parameters are listed in Table 1. Solid lines in panels b and d represent the normalized electron densities of the interfaces along the axis normal to the interface. Dashed lines in panels b and d represent the same electron density profiles as the solid lines with the roughness parameter, σ, set to zero for illustrative purposes.

Three angles, corresponding to rotations about each of the Cartesian axes, are required to specify the orientation of a rigid body in space. Since rotations of the protein about an angle normal to the lipid layer are redundant, only two angles are required to specify the protein orientation.

RESULTS

SOPC/SOPS/DPPtdIns(3)P Monolayer

X-ray reflectivity data from Langmuir monolayers of lipids are typically analyzed using a model for the electron density profile that consists of two slabs sandwiched between bulk aqueous buffer and bulk vapor (*32*), though an alternative method of representing pieces of the lipid by Gaussian profiles is sometimes used (*33*). One slab represents the average electron density in the headgroup region of the lipids, and the other slab represents the average electron density in the tailgroup (acyl group) region (see the dashed line in Figure 3b). Each slab is characterized by a constant electron density ρ throughout its thickness L. The density is smeared at the slab borders to provide a smooth crossover between slabs. This is a physical effect due to thermal fluctuations of the water surface, known as capillary waves, that produces a time-averaged smearing of the profile as measured by X-ray reflectivity. This smearing is characterized by an interfacial roughness (or width) σ. The electron density is determined by fitting the measured data to reflectivity calculated from this model profile.

X-ray reflectivity data for an SOPC/SOPS/DPPtdIns(3)P monolayer at a surface pressure of 25.9 mN/m are shown in Figure 3a. Although this measurement has only a small number of data points, it is consistent with other measurements we have taken with a larger number of data points and is adequate for characterizing the lipid monolayer (as described in Materials and Methods). The measurement shown in Figure 3a preceded the measurement of the bound protein, illustrated in Figure 3c, that will be discussed later. These data for the lipid monolayer were analyzed by a two-slab model for the electron density, given by the equation,

$$\langle\rho(z)\rangle = \frac{\rho_{air} + \rho_{buffer}}{2} + \left(\frac{\rho_{air} - \rho_{tail}}{2}\right)\mathrm{erf}\left(\frac{z}{\sqrt{2\sigma^2}}\right) + \left(\frac{\rho_{tail} - \rho_{head}}{2}\right)\mathrm{erf}\left(\frac{z + L_{tail}}{\sqrt{2\sigma^2}}\right) + \left(\frac{\rho_{head} - \rho_{buffer}}{2}\right)\mathrm{erf}\left(\frac{z + L_{tail} + L_{head}}{\sqrt{2\sigma^2}}\right) \quad (1)$$

where $\mathrm{erf}(z) = (2/\sqrt{\pi})\int_0^z \exp(-t^2)dt$, L_{head} and L_{tail} are the thickness of the headgroup and tailgroup, respectively, ρ_{head} and ρ_{tail} represent the average electron densities (normalized to the electron density of the subphase, $\rho_{buffer} = 0.337$ e$^-$/Å^3) of the headgroup and tailgroup, respectively, ρ_{air} is the electron density of the air and is equal to zero, and σ is the roughness of the surface calculated by capillary wave theory using the measured temperature and surface pressure (*34*, *35*). Note that the dependence of the fit parameters for the SOPC/SOPS/DPPtdIns(3)P monolayer on the uncertainties of the surface pressure ($\pm$1 mN/m) yielded values within the error bars quoted later. The air−tailgroup, tailgroup−headgroup, and headgroup−buffer interfaces were located as follows: $z = 0$, $z = -L_{tail}$, and $z = -(L_{tail} + L_{head})$, respectively. The Parratt algorithm (*31*) was used to calculate the reflectivity from the electron density profile given by eq 1. Fitting the data to the calculated reflectivity yielded values of the fit parameters: L_{head}, L_{tail}, ρ_{head}, and ρ_{tail}.

The fit is shown in Figure 3a (solid line), and the resulting electron density profile is shown in Figure 3b. The fit parameters listed in Table 1 are very similar to parameters we measured several times for SOPC/SOPS/DPPtdIns(3)P monolayers, including measurements with a much higher density of points. The thickness of the tailgroup region, L_{tail}, and the electron density in this region, ρ_{tail}, indicate that the acyl chains were disordered. The high electron density in the headgroup region was due to the presence of the phosphate group. The total thickness of the monolayer was 22 Å, consistent with the dimensions of a phospholipid molecule.

Table 1: Parameters for the SOPC/SOPS/DPPtdIns(3)P Monolayer and Monolayer-Bound p40^{phox}-PX[a]

	SOPC/SOPS/DPPtdIns(3)P	SOPC/SOPS/DPPtdIns(3)P−p40^{phox}-PX		
π_0 (mN/m)		25.9 ± 0.5	26.3 ± 0.5	27.6 ± 0.5
$\Delta\pi$ (mN/m)		4.7 ± 0.5	4.4 ± 0.5	4.0 ± 0.5
L_{tail} (Å)	9.93 ± 0.09	9.3 ± 0.2	10.0 ± 0.2	10.0 ± 0.2
L_{head} (Å)	12.0 ± 0.5	11.0 ± 0.9	11.3 ± 0.7	10.5 ± 1.2
CEN (Å)		33 ± 2	34 ± 2	33 ± 3
ρ_{tail}	0.65 ± 0.02	0.60 ± 0.03	0.60 ± 0.02	0.59 ± 0.02
ρ_{head}	1.26 ± 0.01	1.25 ± 0.02	1.25 ± 0.02	1.23 ± 0.03
COV		0.75 ± 0.07	0.71 ± 0.06	0.57 ± 0.08
σ (Å)	3.3	3.4	3.5	3.5
A_{box} (Å^2)		1890	1890	1890
CEN_{cryst} (Å)		26.5	26.5	26.5
$L_{>CEN}$ (Å)		22.0	22.0	22.0
$A_{protein}$ (Å^2)		2500^{+300}_{-200}	2700 ± 200	3300^{+500}_{-400}
PEN (Å)		9 ± 3	9 ± 3	9 ± 4
χ^2		9.9	7.4	12.4
$\chi^2_{Q_z<0.2}$		8.8	8.5	14.7

[a] The fit parameters for the best fit orientation (Figure 2) ($\theta = 30°$, $\phi = 140°$) for three experiments with different initial lipid pressures are listed. L_{tail}, L_{head}, CEN, ρ_{tail}, ρ_{head}, and COV are fit parameters; σ, $A_{protein}$, and PEN are calculated as described in the text. A_{box}, CEN_{cryst}, and $L_{>CEN}$ are parameters extracted from *Cerius*^{2} (*26*). Normalized electron densities must be multiplied by 0.337 e^-/Å^3 to obtain absolute electron densities. χ^2 is the statistical measure of goodness of fit for the entire range of Q_z; $\chi_{Q_z<0.2}{}^2$ is for a smaller range of Q_z (<0.2 Å^{-1}) that is most sensitive to the protein ordering.

These values are consistent with previous measurements of SOPC and similar lipids in bilayers or Langmuir monolayers. In our previous measurements of the SOPC monolayer at a surface pressure of 24 mN/m (*26*), we reported the headgroup and tailgroup thickness to be 10.5 ± 0.5 and 10.6 ± 0.1 Å, respectively, and the headgroup and tailgroup normalized electron density to be 1.25 ± 0.01 and 0.62 ± 0.01, respectively. There is not much information about the structure of SOPC/SOPS/DPPtdIns(3)P monolayers and bilayers in the literature, but lipid monolayers and bilayers consisting of DPPC (1,2-dipalmitoyl-*sn*-glycero-3-phosphocholine), POPC (1-palmitoyl-2-oleoyl-*sn*-glycero-3-phosphocholine), or DOPC (1,2-dioleoyl-*sn*-glycero-3-phosphocholine) were studied. As discussed in ref *26*, the literature values are consistent with our measurements.

SOPC/SOPS/DPPtdIns(3)P Monolayer with Bound p40^{phox}-PX

Surface Pressure Data. The change in surface pressure $\Delta\pi$ after adsorption of p40^{phox}-PX onto the SOPC/SOPS/DPPtdIns(3)P monolayer is plotted in Figure 4 as a function of initial surface pressure π_0 of the SOPC/SOPS/DPPtdIns(3)P monolayer (see Materials and Methods). Filled circles represent data taken on samples without prior X-ray exposure. Values of $\Delta\pi$ were also measured during three independent experiments at the synchrotron (empty circles in Figure 4) by measuring the pressure after the X-ray reflectivity measurement of the pure SOPC/SOPS/DPPtdIns(3)P monolayer but before the reflectivity measurement of the lipid/protein system. The measured values of $\Delta\pi$ (4.7 mN/m when $\pi_0 = 25.9$ mN/m, 4.4 mN/m when $\pi_0 = 26.3$ mN/m, and 4.0 mN/m when π_0=27.6 mN/m) were consistent with the values measured without prior X-ray exposure.

X-ray Data and Reflectivity Model that Incorporates Protein Crystallography Structure. We carried out three independent X-ray reflectivity experiments for lipid/protein systems with similar initial lipid pressures. X-ray reflectivity data from the p40^{phox}-PX domain bound to a SOPC/SOPS/DPPtdIns(3)P monolayer for the experiment with the lowest initial pressure ($\pi_0 = 25.9$ mN/m) are shown in Figure 3c. In comparison to the reflectivity from the pure SOPC/SOPS/DPPtdIns(3)P monolayer in panel a, an additional peak is located in the low-Q_z region and the highest Q_z data have a different shape. The peak is due to the PX domain bound to the lipid monolayer.

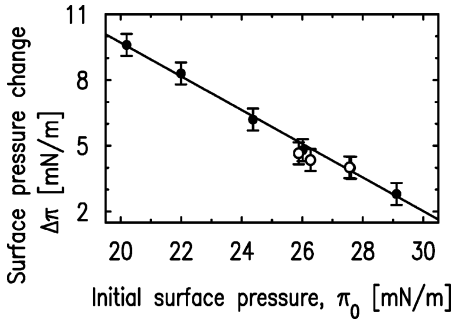

FIGURE 4: Change in surface pressure upon adsorption of p40^{phox}-PX to the SOPC/SOPS/DPPtdIns(3)P monolayer as a function of the initial monolayer pressure prior to adsorption. Filled circles indicate the data measured without X-ray exposure of SOPC/SOPS/DPPtdIns(3)P monolayers as described in Materials and Methods. Empty circles represent the values measured at the synchrotron immediately before measuring the X-ray reflectivity of the lipid/protein system.

The slab model method of analysis, previously applied to reflectivity data measured from proteins bound to Langmuir monolayers of lipids (*20*−*25*), consists of a three-slab model similar to the two-slab model used to analyze the data from the SOPC/SOPS/DPPtdIns(3)P monolayer. In this case, the third slab would represent the bound proteins. The fit to the data and resultant electron density profile from this analysis were very similar to those shown in panels c and d of Figure 3. However, the fit parameters for this slab model (not shown) do not directly determine the angular orientation of the protein or the depth of penetration of the protein into the lipid monolayer. To extract this information, we used a modified reflectivity analysis that utilizes the protein structure determined from X-ray crystallography (*26*).

The X-ray crystallographic structure of p40^{phox}-PX (PDB entry 1H6H) (*10*) was used to model the electron density

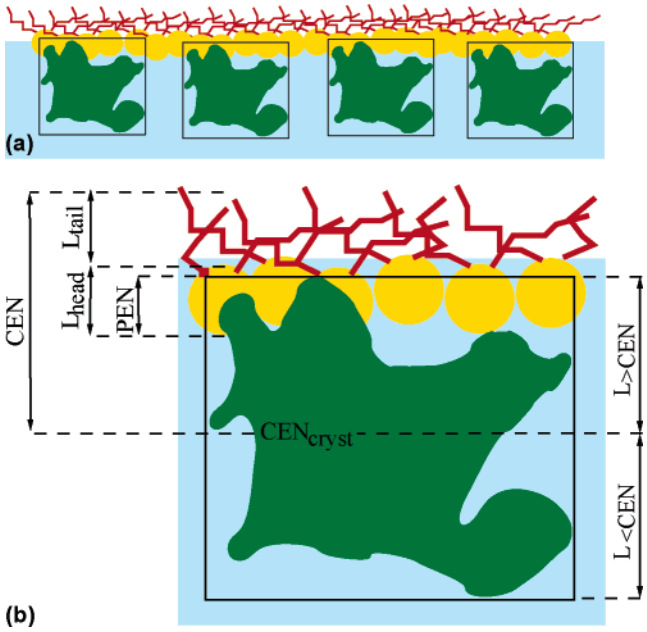

FIGURE 5: (a) Schematic view of the lipid monolayer with the adsorbed proteins enclosed in the smallest possible rectangular boxes. Yellow circles and red curves represent the lipid headgroups and tailgroups, respectively; proteins enclosed in boxes are schematically shown as green objects in black rectangles (the real structure of the protein in its smallest box is shown in Figure 2). The parameters appearing in eq 4 are given in panel b, which is an enlarged version of one of the boxed proteins together with adjacent lipids.

distribution of the p40^{phox}-PX domain. This structure of p40^{phox}-PX was determined with DBuPtdIns(3)P bound to it and, therefore, provided the structure of the site which binds PtdIns(3)P. The p40^{phox}-PX domain studied by X-ray reflectivity is shown in Figure 2. As will be demonstrated, the orientation shown in Figure 2 is the best fit from our analysis. Our best fit orientation is characterized by the following angles: $\theta = 30°$ and $\varphi = 140°$ (see Materials and Methods for the definition of these angles).

To use the structure shown in Figure 2 in the reflectivity analysis, a one-dimensional electron density profile along the z axis, averaged over the $x-y$ directions, must be determined. This protein profile (termed $\langle\rho_{protein\_layer}(z)\rangle$), modified for the presence of buffer, was then situated between the profile for the bulk aqueous buffer and the two slabs that described the lipid monolayer. This combined profile was then used to fit the X-ray reflectivity data. An additional degree of freedom allowed the protein profile to penetrate into the region of the monolayer. The fitting determined the depth of penetration of the protein into the lipid monolayer, the fraction of area of the lipid monolayer with bound protein, and the lipid parameters, for the domain orientation shown in Figure 2 (see ref *26* for details of this analysis). The same procedure was undertaken for different angular orientations of the protein to determine if other orientations could fit the data and, if so, the fit parameters for those orientations.

To account for the presence of buffer that surrounded the protein (i.e., buffer at the same surface depth as the protein), the electron density profile of the protein layer was modeled by enclosing a single protein in the smallest possible rectangular box (Figure 5). Since part of the protein was in the buffer environment, while the rest penetrated the lipid layer, which did not contain buffer, the electron density of the protein in the box was calculated for both protein in a box filled with buffer and protein in an empty box. The interface then consisted of the boxed proteins and the lipid monolayer (Figure 5). Details of the determination of the electron density of the protein in a box were described in our earlier work (*26*). The electron density profile for the protein in the best fit orientation in a box with buffer is shown in Figure S1 of the Supporting Information.

The electron density profile of a protein in a box $\langle\rho_{protein\_box}(z)\rangle$ was used to model the electron density profile of a protein layer [$\langle\rho_{protein\_layer}(z)\rangle$] by introducing the coverage parameter COV, the fraction of surface area occupied by the protein boxes, as

$$\langle\rho_{protein\_layer}(z_p)\rangle = \mathrm{COV}\langle\rho_{protein\_box}(z_p)\rangle \qquad (2)$$

The area per protein ($A_{protein}$) was calculated as (*26*)

$$A_{protein} = A_{box}/\mathrm{COV} \qquad (3)$$

where A_{box} is the area of the side of the box in the $x-y$ plane (parallel to the lipid monolayer). Since the electron density of the buffer was normalized to unity, this expression for $\langle\rho_{protein\_layer}(z)\rangle$ accounted for buffer between the protein boxes that was present when the surface was not fully covered by protein.

The final model for the electron density profile of the lipid/protein system was given by the sum of the electron density profile of the protein layer and the electron density of the lipid layer described by two slabs. The coordinate system was chosen to place the air−tailgroup interface at $z = 0$ and the buffer−protein interface at $z < 0$. The position of the protein with respect to the lipid layer was determined by the parameter CEN, where CEN is the distance between the protein center and the air−tailgroup interface at $z = 0$ (see Figure 5). In this geometry, the penetration (PEN) of the protein into the lipid layer (which measures the distance from the headgroup−buffer interface to the residue of the protein that penetrates most deeply into the lipid layer) was calculated as

$$\mathrm{PEN} = L_{>\mathrm{CEN}} - [\mathrm{CEN} - (L_{tail} + L_{head})] \qquad (4)$$

where $L_{>CEN}$ characterizes the protein length along the z axis measured from the center of the protein to the protein end that penetrates into the lipid. Lengths appearing in eq 4 are shown in Figure 5b. Interfacial roughness was incorporated into the model by convoluting the electron density profile with a Gaussian of width σ, where σ is calculated from capillary wave theory.

The X-ray reflectivity data were fit with reflectivity calculated by the Parratt algorithm applied to the model given above. There were six fitting parameters, four for the lipid layer (L_{head}, L_{tail}, ρ_{head}, and ρ_{tail}) and two for the protein layer (CEN and COV). The fit for the orientation in Figure 2 is shown in panel c of Figure 3 and the corresponding electron density profile in panel d, and fit parameters are listed in Table 1 (in the column labeled $\pi_0 = 25.9$ mN/m). The fit is good throughout the entire range of Q_z. Note that the region of low Q_z is most sensitive to the protein and the region of higher Q_z is sensitive to the lipid structure. The protein

orientation shown in Figure 2 provides the best fit to our data. Fits for other orientations are discussed in the next section.

Approximately three-quarters of the lipid layer was covered by protein (COV = 0.75). Equation 3 was used to determine the area per protein (2500 Å^2). Equation 4 was used to determine a value of 9 ± 3 Å for the penetration of the protein, in this orientation, into the lipid layer. The headgroup and tailgroup densities were reduced by approximately 10% upon protein adsorption. This reduction could be due to re-equilibration of the monolayer/protein system that occurred during stirring.

Analysis of the data for the other two experiments (π_0 = 26.3 mN/m and π_0 = 27.6 mN/m) produced fit parameters for the protein in this orientation that are very similar to those just discussed, except that the protein coverage decreased and the area per protein increased as π_0 increased (see Table 1). Taking into account the penetration values for these three statistically independent measurements yields a net value for the penetration depth of 9 ± 2 Å.

Three loop regions in the p40^{phox}-PX structure were near or penetrated into the lipid monolayer (Figure 2). The loop connecting strands β1 and β2 (residues 33−37) is termed L1, and the loop just before helix α3 (residues 93−97) is termed L3. Loops L1 and L3 are located in the region surrounding the PtdIns(3)P-binding pocket identified by X-ray crystallography (*10*). The loop region just after helix α2 (residues 73−85) is termed L2. Loops L1 and L3 penetrated into the lipid monolayer, while loop L2 did not (Figure 2). Residues Tyr^{94} and Val^{95} (both located in L3) penetrated deepest into the lipid monolayer, with the side chain of Val^{95} extending nearly 9 Å above the headgroup−buffer interface. The backbone of these residues was ∼5 Å above the headgroup−buffer interface, i.e., at the level of the SOPC/SOPS lipid phosphates (see ref *36* for a determination of the distance between the phosphates and the headgroup). The center of the Tyr^{94} ring is also situated at the level of the SOPC/SOPS lipid phosphates. Residues Phe^{35} (L1), Thr^{36} (L1), Lys^{92} (L3), Val^{93} (L3), Val^{97} (L3), and Lys^{98} (L3) were located at the headgroup−buffer interface. None of the L2 loop residues penetrated into the headgroup region. Neither L1, L2, nor L3 penetrated into the tailgroup region.

Protein Orientation and Penetration

To investigate other protein orientations that may be consistent with the X-ray data, the protein was rotated to various orientations defined by angles θ and φ. We explored all combinations of angles θ and φ in 10° steps. Orientations that were not consistent with the following earlier results were excluded. First, the crystal structure of DBuPtdIns(3)P-bound p40^{phox}-PX (PDB entry 1H6H) (*10*) is known. We considered rotations of this DBuPtdIns(3)P-bound p40^{phox}-PX structure. If the orientation of DBuPtdIns(3)P in a particular protein orientation (with respect to the lipid monolayer) was grossly implausible [e.g., the hydrophilic DBuPtdIns(3)P headgroup penetrated into the membrane, while the DBuPtdIns(3)P hydrophobic tails were immersed into the buffer], then that orientation was discarded. Second, the membrane binding affinity (measured by surface plasmon resonance) and the change of surface pressure upon domain binding (measured by monolayer techniques) of p40^{phox}-PX and its mutants were reported by Stahelin et al. (*15*). According to their results, the p40^{phox}-PX domain mutated in the loop region surrounding the PtdIns(3)P-binding pocket (mainly mutation of Phe^{35} to Ala in L1, and mutations of Tyr^{94} to Ala and Val^{95} to Ala in L3) had reduced membrane binding affinity and greatly lowered the change in surface pressure upon domain binding. In contrast, the protein with Leu^{82} mutated to Ala (located in L2) behaved like the wild-type protein, with the same membrane binding affinity and the same change in surface pressure. Stahelin et al. (*15*) concluded that only loops L1 and L3 participate in membrane penetration. If a domain orientation was inconsistent with their results (e.g., loop L2 was deeper in the membrane than loops L1 and L3), then that orientation was discarded. Orientations inconsistent with the results discussed above are indicated with blue squares in Figure 6.

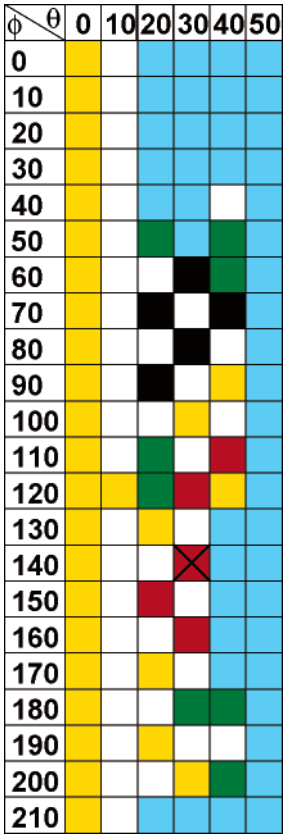

FIGURE 6: Goodness of fit for various orientations. Each appropriately colored square corresponds to an orientation which was used to fit the data. The red square with an X corresponds to the best fit orientation. Orientations yielding good fits (within 1.3 standard deviations of the best fit) are shown as red squares without an X. Orientations yielding fits that lie between 1.6 and 3.3 standard deviations are shown as yellow squares. Green and black squares indicate fits that deviate from the best fit by at least 3.3 and 4 standard deviations, respectively. Blue squares stand for orientations which were discarded due to inconsistency with earlier results (see the text). Therefore, all orientations with a θ of ≥50° and a φ of ≥210° (with the exception of orientations characterized by θ values of 0° and 10°) were discarded. When θ = 0°, all values of φ yield the same orientation.

The orientations chosen for X-ray data analysis in Figure 6 are depicted as red, yellow, green, and black squares. These orientations were analyzed by repeating the procedure described in the previous section. The goodness of fit (χ^2) followed the same trend for the three experiments with different initial pressures. The color representation of the

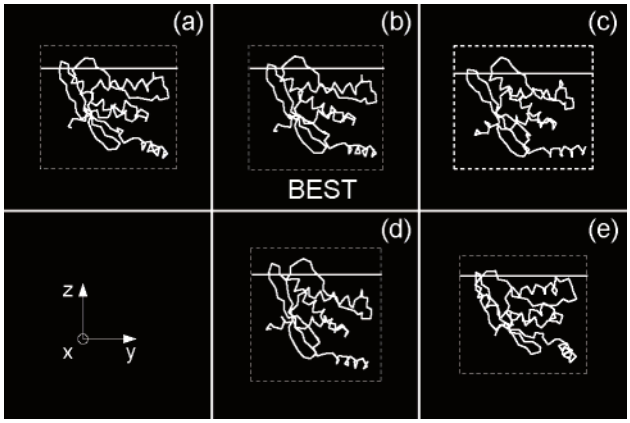

FIGURE 7: Protein orientations that produced the best fit (b) and other fits with a statistical deviation of approximately one standard deviation from the best fit (see Table 2): (a) $\theta = 30°$ and $\varphi = 120°$, (b) $\theta = 30°$ and $\varphi = 140°$, (c) $\theta = 30°$ and $\varphi = 160°$, (d) $\theta = 20°$ and $\varphi = 150°$, and (e) $\theta = 40°$ and $\varphi = 110°$. The white solid lines indicate the border between the lipid headgroups and the buffer. The positions of the white lines were calculated for each orientation via eq 4. The part of the protein above the lines penetrates into the SOPC/SOPS/DPPtdIns(3)P monolayer.

goodness of fits for the investigated orientations is shown in Figure 6. The red squares represent fits within 1.3 standard deviations of the best fit. Yellow squares denote orientations yielding fits that lay between 1.6 and 3.3 standard deviations from the best fit. Green and black squares represent fits that deviate from the best fit by greater than 3.3 and 4 standard deviations, respectively. Representative fits with these different standard deviations from the best fit are shown in Figure S2 of the Supporting Information (residuals of these fits are shown in Figure S3 of the Supporting Information). White squares represent orientations that were not analyzed. Orientations defined by a θ of 10° and various values of φ are very similar to each other. Therefore, we analyzed only one of these orientations ($\theta = 10°$, $\varphi = 120°$), since all others would yield similar fits. The region in the $\theta-\varphi$ plane that corresponds to orientations producing good fits (red squares) can be parametrized by

$$\theta = 30° \pm \Delta\theta$$
$$\phi = (-2\theta + 200°) \pm \Delta\phi \quad (5)$$

where $\theta = 30°$ and $\varphi = (-2\theta + 200°) = 140°$ is the center of the region. The region is delimited by a $\Delta\theta$ of 10° and $\Delta\varphi$, where $\Delta\varphi = 30°$ when $\theta = 30°$ and $\Delta\varphi = 10°$ when $\theta = 20°$ or 40°. The orientation defined by a θ of 30° and a φ of 140° is located in the center of the good fit region and produced the best fit for all three experiments. Orientations that provided fits to the data within 1.3 standard deviations of the best fit (red squares in Figure 6) are shown in Figure 7, with the best fit orientation shown in panel b of Figure 7 (and also in Figure 2).

The fit parameters for the orientations in Figure 7 are listed in Table 2. The values were determined for the experiment for which $\pi_0 = 26.3$ mN/m. Fit parameters for the other two experiments (not shown) are very similar, except for the protein coverage. Two different values of χ^2 were considered, one that measured the goodness of fit over the entire range of Q_z (denoted χ^2) and the other that measured the goodness of fit over a smaller range of Q_z (<0.2 Å^{-1}) (denoted $\chi^2_{Q_z<0.2}$) that was most sensitive to the protein ordering. The best fit orientation [$\theta = 30°$, $\varphi = 140°$ (Figure 7b)] has the lowest values of χ^2 and $\chi^2_{Q_z<0.2}$. Table 2 also indicates the statistical deviation of these fits from the best fit.

DISCUSSION

In this work, synchrotron X-ray reflectivity was used to investigate the orientation and position of the p40^{phox}-PX domain bound to an SOPC/SOPS/PtdIns(3)P monolayer at the air−water interface. X-ray reflectivity from the monolayer was measured before and after a protein solution was injected into the subphase. The SOPC/SOPS/PtdIns(3)P monolayer was modeled by two slabs; one slab represented the headgroup region and the other the tailgroup region of the lipids. Although a third slab could have been used to model the p40^{phox}-PX domain bound to the SOPC/SOPS/PtdIns(3)P monolayer, this simple model is incapable of determining directly the orientation and penetration of the domain. To determine this information from the reflectivity measurements, a model that utilized the reported crystal structure of p40^{phox}-PX was used. The use of the crystal structure for modeling of the SOPC/SOPS/PtdIns(3)P monolayer-bound p40^{phox}-PX is justified by the following observations. First, solution NMR structure determination by Lu et al. (*37*) showed that binding of the Vam7p-PX domain (PDB entry 1KMD) by DBuPtdIns(3)P caused only small magnitude amide chemical shift changes, suggesting minor structural changes. Also, the similarity between the crystal structure of the p40^{phox}-PX and the solution structure of Vam7p-PX indicates that the domain structure is robust and independent of a crystalline or liquid environment.

Four fit parameters characterized the SOPC/SOPS/PtdIns(3)P layer, and two additional parameters were used to model the protein domain. The parameter CEN determined the depth of penetration of p40^{phox}-PX into the SOPC/SOPS/PtdIns(3)P monolayer, and coverage parameter COV characterized the area fraction of the SOPC/SOPS/PtdIns(3)P monolayer with the bound proteins. The orientation shown in Figure 2, as well as in Figure 7b, provided the best fit to the reflectivity data. Of 26 additional orientations that were investigated, four produced good fits (Figure 7). The best fit orientation ($\theta = 30°$, $\varphi = 140°$) is at the center of a region in the $\theta-\varphi$ plane that produced good fits (see Figure 6, red squares). The orientation suggested earlier by Stahelin et al. (*15*) ($\theta = 32°$, $\varphi = 122°$) is also located within this region.

In all orientations that produced good fits, loops L1 and L3 penetrated into the lipid monolayer, but not loop L2. The depth of protein penetration was 9 ± 2 Å, as measured from the lipid headgroup−buffer interface. This value, which represents the first membrane penetration depth determined for a PI binding domain by a quantitative analysis, indicates that the protein domain penetrates into the headgroup region, but not deeply into the hydrocarbon region of the monolayer. This penetration depth is smaller than that observed for the hydrophobic residues of the cPLA$_2$α-C2 domain determined by the X-ray reflectivity analysis under similar conditions (*26*).

Our best fit model showing partial membrane penetration of the p40^{phox}-PX domain places positively charged residues Lys^{92} and Lys^{98} near the phosphate groups of SOPC and SOPS, which produces a favorable electrostatic contribution

Table 2: Parameters for the SOPC/SOPS/DPPtdIns(3)P Monolayer and Monolayer-Bound p40^{phox}-PX[a]

θ (deg)	ϕ (deg)	L_{tail} (Å)	L_{head} (Å)	CEN (Å)	ρ_{tail}	ρ_{head}	COV	PEN (±3 Å)	χ^2	$\chi^2_{Q_z<0.2}$
30	**140**	**10.0**	**11.3**	**34**	**0.60**	**1.25**	**0.71**	**9**	**7.4**	**8.5**
30	120	10.0	11.7	34	0.58	1.25	0.70	9	8.2 (1.0 SD)	9.9 (1.0 SD)
30	160	9.9	11.1	34	0.59	1.24	0.71	11	9.0 (1.2 SD)	9.4 (0.9 SD)
20	150	10.1	12.0	36	0.61	1.26	0.66	11	8.9 (1.2 SD)	10.9 (1.2 SD)
40	110	10.1	11.8	33	0.59	1.27	0.76	8	8.7 (1.1 SD)	9.6 (1.0 SD)

[a] Parameters for the orientations that fit the data well (those shown in Figure 7 for the experiment with the initial lipid pressure, π_0, of 26.3 mN/m) are shown. Parameters for two other experiments (not shown) are very similar, except for the coverage parameter (COV). L_{tail}, L_{head}, CEN, ρ_{tail}, ρ_{head}, and COV are fit parameters; PEN is calculated as described in the text. Normalized electron densities must be multiplied by 0.337 e^-/Å^3 to obtain absolute electron densities. χ^2 is the statistical measure of the goodness of fit for the entire range of Q_z; $\chi^2_{Q_z<0.2}$ is for a smaller range of Q_z (<0.2 Å^{-1}) that is most sensitive to the protein ordering. The values in parentheses after the χ^2 values indicate the deviation from the best fit, in units of standard deviations (SD). Parameters for the best fit orientation defined by a θ of 30° and a ϕ of 140° are shown in bold.

to the binding. Electrostatic potential calculations for the p40^{phox}-PX domain in the absence and presence of the PtdIns(3)P headgroup indicate that binding of the p40^{phox}-PX domain to the PtdIns(3)P binding pocket greatly reduces a strong positive electrostatic potential surrounding Tyr^{94} and Val^{95}, which in turn promotes their membrane penetration by decreasing the dehydration penalty for membrane penetration (*15*). The proximity of Lys^{92} and Lys^{98} to the lipid phosphate groups in our best fit orientation should also reduce the positive potential surrounding Tyr^{94} and Val^{95} and thus lower the energetic barrier opposing the penetration of these residues into the low-dielectric membrane interface.

Our data do not allow us to determine if the location of PtdIns(3)P in our experiment is the same as that determined for the crystal sample of DBuPtdIns(3)P-bound p40^{phox}-PX (without a lipid membrane). According to Bravo et al. (*10*), Arg^{58} directly interacts with the 3-phosphate of DBuPtdIns(3)P and thus plays a critical role in PtdIns(3)P binding. The finding that the mutation of Arg^{58} to Gln resulted in a loss of binding to not only monomeric DBuPtdIns(3)P (*10*) but also to POPC/POPE/DPPtdIns(3)P monolayers and bilayers (POPE stands for 1-palmitoyl-2-oleoyl-*sn*-glycero-3-phosphoethanolamine) (*15*) supports the notion that the position of the DBuPtdIns(3)P headgroup in the binding site of the p40^{phox}-PX domain as determined from crystal samples (in the absence of a lipid membrane) is similar to the position of DPPtdIns(3)P bound to p40^{phox}-PX adsorbed to a lipid monolayer or to lipid vesicles. If the arrangement of the binding pocket and the PtdIns(3)P in our samples is the same as that described by Bravo et al. (*10*) for DBuPtdIns(3)P bound to p40^{phox}-PX, then a DPPtdIns(3)P molecule must be drawn out of the lipid plane by 5 Å so that its tailgroup is moved slightly into the region of the SOPC and SOPS headgroups. The 1-phosphate of DPPtdIns(3)P is then located approximately 1 Å on the headgroup side of the SOPC/SOPS headgroup−buffer interface, and the 3-phosphate of DPPtdIns(3)P is located approximately 4 Å on the buffer side of the headgroup−buffer interface. Although it is difficult to estimate the exact distance PtdIns(3)P would travel upon membrane binding of the p40^{phox}-PX domain, due to the lack of structural information about PtdIns(3)P or any PI in lipid monolayers or bilayers, these results collectively suggest that PtdIns(3)P moves out of the lipid bilayer plane to enter the PtdIns(3)P-binding pocket of the p40^{phox}-PX domain.

On the basis of biophysical studies on a series of PI-binding domains, Cho and Stahelin proposed a general mechanism for the membrane binding of PI-binding domains (*38*). In this mechanism, a domain initially adsorbs to the membrane surface through nonspecific electrostatic interactions or Trp−zwitterionic headgroup interactions. This is followed by binding of PI to the domain, which typically induces partial membrane penetration of the domain. It should be noted that the membrane-bound orientation and membrane penetration depth of the p40^{phox}-PX domain bound to a non-PtdIns(3)P-containing monolayer could not be analyzed in this study due to the low surface coverage of proteins. Therefore, how the p40^{phox}-PX domain initially binds to the anionic membrane surface and how the subsequent PtdIns(3)P binding induces the membrane penetration of the protein remain unknown. Nevertheless, this study shows that binding of PtdIns(3)P to its pocket, which seems to require the out-of-plane migration of PtdIns(3)P, mediates partial membrane penetration of the p40^{phox}-PX domain. It is tempting to postulate that initial long-range electrostatic interactions lead to only transient membrane adsorption of the domain, whereas PtdIns(3)P-mediated partial membrane penetration allows shorter-range specific interactions, including hydrogen bonds, between surface cationic residues of p40^{phox}-PX and anionic phosphate groups of lipids as well as partial sequestration of hydrophobic side chains in the low-dielectric membrane interface. Both effects would result in higher membrane affinity and longer membrane residence. Further studies on other PX domains and PI-binding proteins which allow data analysis on proteins bound to both PI-containing and non-PI-containing monolayers will lead to a better understanding of how PIs mediate the membrane penetration of these important classes of proteins.

ACKNOWLEDGMENT

We acknowledge Fei Long for his help with fluorescence microscopy measurements and buffer preparation and Aleksey Tikhonov, the X19C beamline scientist.

SUPPORTING INFORMATION AVAILABLE

An example of the electron density profile for the case of the protein in the best fit orientation in a box with buffer (Figure S1), representative fits for the different colored boxes in Figure 6 (Figure S2), and residuals for these different fits (Figure S3). This material is available free of charge via the Internet at http://pubs.acs.org.

REFERENCES

1. Cho, W. (2001) Membrane targeting by C1 and C2 domains, *J. Biol. Chem. 276*, 32407−32410.

2. Hurley, J. H., and Misra, S. (2000) Signaling and subcellular targeting by membrane-binding domains, *Annu. Rev. Biophys. Biomol. Struct. 29*, 49−79.
3. Hurley, J. H., and Meyer, T. (2000) Subcellular targeting by membrane lipids, *Curr. Opin. Cell Biol. 13*, 146−152.
4. Cullen, P. J., Cozier, G. E., Banting, G., and Mellor, H. (2001) Modular phosphoinositidebinding domains: Their role in signaling and membrane trafficking, *Curr. Biol. 11*, R882−R893.
5. Itoh, T., and Takenawa, T. (2002) Phosphoinositide-binding domains. Functional units for temporal and spatial regulation of intracellular signalling, *Cell. Signalling 14*, 733−743.
6. Stahelin, R. V., Long, F., Diraviyam, K., Bruzik, K. S., Murray, D., and Cho, W. (2002) Phosphatidylinositol 3-phosphate induces the membrane penetration of the FYVE domains of Vps27p and Hrs, *J. Biol. Chem. 277*, 26379−26388.
7. Karathanassis, D., Stahelin, R. V., Bravo, J., Perisic, O., Pacold, C. M., Cho, W., and Williams, R. L. (2002) Binding of the PX domain of p47(phox) to phosphatidylinositol 3, 4-bisphosphate and phosphatidic acid is masked by an intramolecular interaction, *EMBO J. 21*, 5057−5068.
8. Stahelin, R. V., Long, R., Peters, B. J., Murray, D., Camilli, P. D., McMahon, H. T., and Cho, W. (2003) Contrasting membrane interaction mechanisms of AP180 N-terminal homology (ANTH) and epsin N-terminal homology (ENTH) domains, *J. Biol. Chem. 278*, 28993.
9. Ponting, C. P. (1996) Novel domains in NADPH oxidase subunits, sorting nexins, and PtdIns 3-kinases: Binding partners of SH3 domains, *Protein Sci. 5*, 2353−2357.
10. Bravo, J., Karathanassis, D., Pacold, C. M., Pacold, M. E., Ellson, C. D., Anderson, K. E., Butler, P. J. G., Lavenir, I., Perisic, O., Hawkins, P. T., Stephens, L., and Williams, R. L. (2001) The crystal structure of the PX domain from p40^{phox}-PX bound to phosphatidylinositol 3-phosphate, *Mol. Cell 8*, 829−839.
11. Zhan, Y., Virbasius, J. V., Song, X., Pomerleau, D. P., and Zhou, G. W. (2002) The p40(phox) and p47(phox) PX domains of NADPH oxidase target cell membranes via direct and indirect recruitment by phosphoinositides, *J. Biol. Chem. 277*, 4512−4518.
12. Ellson, C. D., Gobert-Gosse, S., Anderson, K. E., Davidson, K., Erdjument-Bromage, H., Tempst, P., Thuring, J. W., Cooper, M. A., Lim, Z.-Y., Holmes, A. B., Gaffney, P. R., Coadwell, J., Chilvers, E. R., Hawkins, P. T., and Stephens, L. R. (2001) PtdIns-(3)P regulates the neutrophil oxidase complex by binding to the PX domain of p40phox, *Nat. Cell Biol. 3*, 679−682.
13. Cheever, M. L., Sato, T. K., de Beer, T., Kutateladze, T. G., Emr, S. D., and Overduin, M. (2001) Phox domain interaction with PtdIns(3)P targets the Vam7 t-SNARE to vacuole membranes, *Nat. Cell Biol. 3*, 613−618.
14. Xu, Y., Hortsman, H., Seet, L. F., Wong, S. H., and Hong, W. (2001) SNX3 regulates endosomal function through its PX-domain-mediated interaction with PtdIns(3)P, *Nat. Cell Biol. 3*, 658−666.
15. Stahelin, R. V., Burian, A., Bruzik, K. S., Murray, D., and Cho, W. (2003) Membrane binding mechanisms of the PX domains of NADPH oxidase p40^{phox}-PX and p47^{phox}-PX, *J. Biol. Chem. 278*, 14469−14479.
16. Kutateladze, T. G., Capelluto, D. G. S., Ferguson, C. G., Cheever, M. L., Kutateladze, A. G., Prestwich, G. D., and Overduin, M. (2004) Multivalent mechanism of membrane insertion by the FYVE domain, *J. Biol. Chem. 279*, 3050−3057.
17. Brunecky, R., Lee, S., Rzepecki, P. W., Overduin, M., Prestwich, G. D., Kutateladze, A. G., and Kutateladze, T. G. (2005) Investigation of the binding geometry of a peripheral membrane protein, *Biochemistry 44*, 16064−16071.
18. Frazier, A. A., Wisner, M. A., Malmberg, N. J., Victor, K. G., Fanucci, G. E., Nalefski, E. A., Falke, J. J., and Cafiso, D. S. (2002) Membrane orientation and position of the C2 domain from cPLA2 by site-directed spin labeling, *Biochemistry 41*, 6282−6292.
19. Malmberg, N. J., Van Buskirk, D. R., and Falke, J. J. (2003) Membrane-docking loops of the cPLA2 C2 domain: Detailed structural analysis of the protein-membrane interface via site-directed spin-labeling, *Biochemistry 42*, 13227−13240.
20. Bitto, E., Li, M., Tikhonov, A. M., Schlossman, M. L., and Cho, W. (2000) Mechanism of annexin I-mediated membrane aggregation, *Biochemistry 39*, 13469−13477.
21. Lee, K. Y. C., Majewski, J., Kuhl, T. L., Howes, P. B., Kjaer, K., Lipp, M. M., Waring, A. J., Zasadzinski, J. A., and Smith, G. S. (2001) Synchrotron X-ray study of lung surfactant-specific protein SP-B in lipid monolayers, *Biophys. J. 81*, 572−585.
22. Weygand, M., Wetzer, B., Pum, D., Sleytr, U. B., Cuvillier, N., Kjaer, K., Howes, P. B., and Lösche, M. (1999) Bacterial S-layer protein coupling to lipids: X-ray reflectivity and grazing incidence diffraction studies, *Biophys. J. 76*, 458−468.
23. Möhwald, H., Balts, H., Schwendler, M., Helm, C. A., Brezesinski, G., and Haas, H. (1995) Phospholipid and protein monolayers, *Jpn. J. Appl. Phys. 34*, 3906−3913.
24. Gidalevitz, D., Huang, Z., and Rice, S. A. (1999) Protein folding at the air-water interface studied with X-ray reflectivity, *Proc. Natl. Acad. Sci. U.S.A. 96*, 2608−2611.
25. Gidalevitz, D., Ishitsuka, Y., Muresan, A. S., Konovalov, O., Waring, A. J., Lehrer, R. I., and Lee, K. Y. C. (2003) Interaction of antimicrobial peptide protegrin with biomembranes, *Proc. Natl. Acad. Sci. U.S.A. 100*, 6302−6307.
26. Málková, Š., Long, F., Stahelin, R. V., Pingali, S. V., Murray, D., Cho, W., and Schlossman, M. L. (2005) X-ray reflectivity studies of cPLA2α-C2 Domains Adsorbed onto Langmuir Monolayers of SOPC, *Biophys. J. 89*, 1861−1873.
27. Bruzik, K. S., and Kubiak, R. J. (1995) General synthesis of phosphatidylinositol 3-phosphates, *Tetrahedron Lett. 36*, 2415−2418.
28. Bittova, L., Sumandea, M., and Cho, W. (1999) A structure-function study of the C2 domain of cytosolic phospholipase A2, *J. Biol. Chem. 274*, 9665−9672.
29. Schlossman, M. L., Synal, D., Guan, Y., Meron, M., SheaMcGarthy, G., Huang, Z., Acero, A., Williams, S. M., Rice, S. A., and Viccaro, P. J. (1997) A synchrotron X-ray liquid surface spectrometer, *Rev. Sci. Instrum. 68*, 4372−4384.
30. Born, M., and Wolf, E. (1980) *Principles of Optics*, Pergamon Press, Oxford, U.K.
31. Parratt, L. G. (1954) Surface studies of solids by total reflection of X-rays, *Phys. Rev. 95*, 359−369.
32. Als-Nielsen, J., and McMorrow, D. (2000) *Elements of Modern X-ray Physics*, John Wiley and Sons Ltd., Chichester, U.K.
33. Lösche, M. (2002) Surface-sensitive X-ray and neutron scattering characterization of planar lipid model membranes and lipid/peptide interactions, in *Peptide-Lipid Interactions, Current Topics in Membranes* (McIntosh, T. J., and Simon, S. A., Eds.) pp 118−163, Academic Press, Chichester, U.K.
34. Buff, F. P., Lovett, R. A., and Stillinger, F. H. (1965) Interfacial density profile for fluids in the critical region, *Phys. Rev. Lett. 15*, 621−623.
35. Mitrinović, D. M., Tikhonov, A. M., Li, M., Huang, Z., and Schlossman, M. L. (2000) Noncapillary-wave structure at the water-alkane interface, *Phys. Rev. Lett. 85*, 582−585.
36. Wiener, M. C., and White, S. H. (1992) Structure of a fluid dioleoylphosphatidylcholine bilayer determined by joint refinement of X-ray and neutron diffraction data. III. Complete structure, *Biophys. J. 61*, 434−447.
37. Lu, J., Garcia, J., Dulubova, I., Südhof, T. C., and Rizo, J. (2002) Solution structure of the Vam7p PX domain, *Biochemistry 41*, 5956−5962.
38. Cho, W., and Stahelin, R. V. (2005) Membrane-protein interactions in cell signaling and membrane trafficking, *Annu. Rev. Biophys. Biomol. Struct. 34*, 11951.

BI061133L